

# A multi-messenger search for exotic field emission with a global magnetometer network

Sami S. Khamis,<sup>1,\*</sup> Ibrahim A. Sulai,<sup>2</sup> Paul Hamilton,<sup>1</sup> S. Afach,<sup>3,4,5</sup> B. C. Buchler,<sup>6</sup> D. Budker,<sup>3,4,5,7</sup> N. L. Figueroa,<sup>3,4,5</sup> R. Folman,<sup>8</sup> D. Gavilán-Martín,<sup>3,4,5</sup> M. Givon,<sup>8</sup> Z. D. Grujić,<sup>9</sup> H. Guo,<sup>10</sup> M. P. Hedges,<sup>11</sup> D. F. Jackson Kimball,<sup>12</sup> D. Kim,<sup>13,14,†</sup> E. Klinger,<sup>15</sup> T. Kornack,<sup>16</sup> A. Kryemadhi,<sup>17</sup> N. Kukowski,<sup>18</sup> G. Łukasiewicz,<sup>19,20</sup> H. Masia-Roig,<sup>3,4,5</sup> M. Padniuk,<sup>19</sup> C. A. Palm,<sup>12</sup> S. Y. Park,<sup>21,‡</sup> X. Peng,<sup>10</sup> M. Pospelov,<sup>22,23</sup> S. Pustelny,<sup>19</sup> Y. Rosenzweig,<sup>8</sup> O. M. Ruimi,<sup>24,3,4,5</sup> P. C. Segura,<sup>21,§</sup> T. Scholtes,<sup>25</sup> Y. K. Semertzidis,<sup>13,14</sup> Y. C. Shin,<sup>13</sup> J. E. Stalnaker,<sup>21</sup> D. Tandon,<sup>21,¶</sup> A. Weis,<sup>26</sup> A. Wickenbrock,<sup>3,4,5</sup> T. Wilson,<sup>12,\*\*</sup> T. Wu,<sup>10</sup> J. Zhang,<sup>10</sup> and Y. Zhao<sup>10</sup>

<sup>1</sup>*Department of Physics and Astronomy, University of California, Los Angeles, California 90095, USA*

<sup>2</sup>*Department of Physics and Astronomy, Bucknell University, Lewisburg, Pennsylvania 17837, USA*

<sup>3</sup>*Helmholtz Institute Mainz, 55099 Mainz, Germany*

<sup>4</sup>*GSI Helmholtzzentrum für Schwerionenforschung GmbH, 64291 Darmstadt, Germany*

<sup>5</sup>*Johannes Gutenberg-Universität Mainz, 55128 Mainz, Germany*

<sup>6</sup>*Research School of Physics, Australian National University, Canberra ACT 2601, Australia*

<sup>7</sup>*Department of Physics, University of California, Berkeley, California 94720, USA*

<sup>8</sup>*Department of Physics, Ben-Gurion University of the Negev, Be'er Sheva 84105, Israel*

<sup>9</sup>*Institute of Physics Belgrade, University of Belgrade, 11080 Belgrade, Serbia*

<sup>10</sup>*State Key Laboratory of Advanced Optical Communication Systems and Networks, Department of Electronics, and Center for Quantum Information Technology, Peking University, Beijing 100871, China*

<sup>11</sup>*Centre for Quantum Computation and Communication Technology,*

*Research School of Physics, The Australian National University, Acton 2601, Australia*

<sup>12</sup>*Department of Physics, California State University – East Bay, Hayward, California 94542-3084, USA*

<sup>13</sup>*Center for Axion and Precision Physics Research, IBS, Daejeon 34051, Republic of Korea*

<sup>14</sup>*Department of Physics, KAIST, Daejeon 34141, Republic of Korea*

<sup>15</sup>*Institut FEMTO-ST – UMR 6174 CNRS, SupMicroTech-ENSMM, Université de Franche-Comté, 25030 Besançon, France*

<sup>16</sup>*Twinleaf LLC, 300 Deer Creek Drive, Plainsboro, NJ 08536, USA*

<sup>17</sup>*Department of Computing, Math & Physics, Messiah University, Mechanicsburg PA 17055, USA*

<sup>18</sup>*Friedrich Schiller University Jena, Institute of Geosciences, Burgweg 11, D-07749 Jena, Germany*

<sup>19</sup>*Institute of Physics, Jagiellonian University in Krakow,*

*prof. Stanisława Łojasiewicza 11, 30-348, Kraków, Poland*

<sup>20</sup>*Jagiellonian University, Doctoral School of Exact and Natural Sciences, Łojasiewicza 11, 30-348, Kraków, Poland*

<sup>21</sup>*Department of Physics and Astronomy, Oberlin College, Oberlin, OH 44074, USA*

<sup>22</sup>*School of Physics and Astronomy, University of Minnesota, Minneapolis, MN 55455, USA*

<sup>23</sup>*William I. Fine Theoretical Physics Institute, School of Physics and Astronomy, University of Minnesota, Minneapolis, MN 55455, USA*

<sup>24</sup>*Racah Institute of Physics, Hebrew University of Jerusalem, Jerusalem 9190401, Israel*

<sup>25</sup>*Leibniz Institute of Photonic Technology, Albert-Einstein-Straße 9, D-07745 Jena, Germany*

<sup>26</sup>*Physics Department, University of Fribourg, CH-1700 Fribourg, Switzerland*

(Dated: July 22, 2024)

We present an analysis method to search for exotic low-mass field (ELF) bursts generated during large energy astrophysical events such as supernovae, binary black hole or binary neutron star mergers, and fast radio bursts using the Global Network of Optical Magnetometers for Exotic physics searches (GNOME). In our model, the associated gravitational waves or electromagnetic signals herald the arrival of the ELF burst that interacts via coupling to the spin of fermions in the magnetometers. This enables GNOME to serve as a tool for multi-messenger astronomy. The algorithm employs a model-agnostic excess-power method to identify network-wide candidate events to be subjected to a model-dependent generalized likelihood-ratio test to determine their statistical significance. We perform the first search with this technique on GNOME data coincident with the binary black hole merger S200311bg detected by LIGO/Virgo on the 11th of March 2020 and find no significant events. We place the first lab-based limits on combinations of ELF production and coupling parameters.

\* [skhamis@physics.ucla.edu](mailto:skhamis@physics.ucla.edu)

† present address: Mechatronics Research, Samsung Electronics, Hwaseong, 18448, South Korea

‡ present address: Department of Physics, University of Colorado, Boulder, Colorado, 80309, USA

§ present address: Department of Physics, Harvard University, Cambridge, Massachusetts, 02138, USA

¶ present address: Department of Physics, Stanford University, Stanford, California, 94305, USA

\*\* present address: Department of Physics, University of Illinois Urbana-Champaign, Urbana, Illinois, 61801, USA

## I. INTRODUCTION

Many extensions of the Standard Model posit the existence of new scalar or pseudoscalar fields with light ( $m \ll 1 \text{ keV}/c^2$ ) quanta, such as axions and axion-like particles (ALPs) [1–3]. In this work, we describe a method to search for light, ultra-relativistic scalar fields triggered by an astrophysical event using the Global Network of Optical Magnetometers for Exotic physics searches (GNOME). Following [4], we refer to these fields as exotic low-mass fields (ELFs). ELFs are postulated to be generated during large energy astrophysical events such as supernovae [5], binary black hole (BBH) or binary neutron star mergers [6], and fast radio bursts (FRB) [7]. The detection of associated gravitational waves (GW) or electromagnetic (EM) signals herald the ELF signal arrival on Earth, and also indicates the GW/EM and ELF source location in the sky. By searching for signatures of the emissions from known sources shortly after a GW or EM trigger, we set limits on possible ELF production and coupling parameters associated with the observed astrophysical event.

The production mechanism of ELFs is an open question [6, 8–11]. Black holes may be surrounded by clouds of exotic bosons, with up to 10% of the black hole mass in the clouds. Theories of scalar-tensor gravity [12] describe cases of black holes and neutron stars being immersed in scalar fields. Such scenarios suggest that modes of these scalar fields may be excited during BBH or binary neutron star mergers [13]. To set limits on ELF properties, we proceed with the following generic assumptions: (1) Some high-energy astrophysical event emits a spherical wave packet of the ELF  $\phi(r)$  from a known location at distance  $R$  from Earth. (2) The emitted wave packet carries away total energy  $\Delta E$ , where  $\Delta E/\varepsilon_0 \gg 1$  with  $\varepsilon_0$  being the energy of an ELF quanta. Given the assumptions above, the ELF will have high mode occupation number and hence they are treated as classical phase-coherent waves.

This manuscript is organized as follows. In Sec. II, we recall the characteristics of an ELF pulse, its propagation, and its coupling to atomic magnetometers. In Sec. III, we describe the GNOME network. In Sec. IV, we present our two-stage analysis pipeline. First, we look for large excess power in the network at particular times and frequencies. We then perform likelihood-ratio tests using the characteristics of the individual stations to determine the significance of possible events compared to time-shifted data, where we expect no signals. We perform the same test on injected signals to calibrate the network response to a known ELF signal. Finally, in Sec. V, we present results for one search target: the BBH merger S200311bg detected by LIGO/Virgo [14].

## II. MODELS FOR ELF PROPAGATION AND DETECTION

### A. Propagation

We start with a cartoon picture for the ELF-signal propagation as shown in Fig. 1. An ELF wave packet is released at the time of an astrophysical event, which emits a GW or EM pulse. As it travels towards the sensors on Earth, the wave packet disperses while conserving its total energy. This leads to an observed frequency chirp at the detector as discussed in more detail below.

Formally, the scalar ELF  $\phi$  can be described by the Klein-Gordon equation [15]. In the case of spherical symmetry, this has 1D solutions of the form  $\phi(r, t) \propto \exp(ikr \pm i\omega t)/r$ , where the frequency  $\omega(k) = [(ck)^2 + (mc^2/\hbar)^2]^{1/2}$  follows the relativistic dispersion relation for the wavenumber  $k$ , the momentum  $\hbar k$ , and the mass of the quanta of the scalar field  $m$ .

Following the derivation in Ref. [4], we consider an ELF pulse having total energy  $\Delta E$ , and assume it has a Gaussian envelope with central ELF frequency  $\omega_0$  and temporal length  $\tau_0$ . After propagation through space, the ELF pulse arrives at Earth with a delay  $\delta t$  after the GW/EM pulse. The waveform at the detector will take the form:

$$\phi(t) \approx \frac{A_0}{R} \sqrt{\frac{\tau_0}{\tau}} \exp\left(-\frac{(t-t_s)^2}{2\tau^2}\right) \cos\left[\omega_0(t-t_s) - \frac{\omega_0}{4\delta t}(t-t_s)^2\right], \quad (1)$$

where  $t_s$  is the time of arrival of the ELF pulse,  $\tau$  is the temporal length at the detector,  $R$  is the distance from the source, and the amplitude  $A_0$  is given by:

$$A_0 \approx \frac{1}{\pi^{1/4}} \left( \frac{1}{\omega_0} \sqrt{\frac{c\Delta E}{2\pi\tau_0}} \right). \quad (2)$$

The second term in the cosine argument of Eq. (1) comes from dispersion of the frequency components of the pulse, leading to a chirped signal.

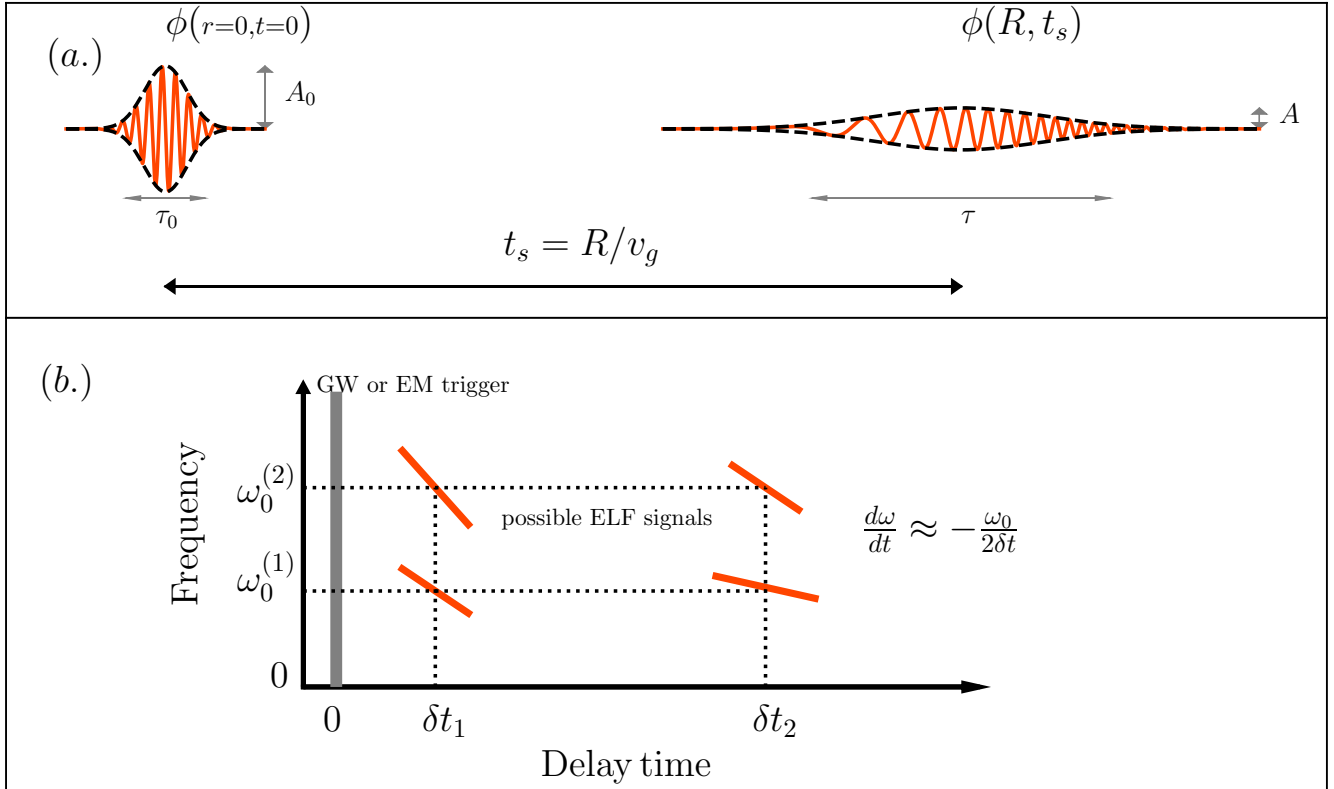


FIG. 1. ELF propagation and signal characteristics. (a) An ELF wave packet,  $\phi(r, t)$ , emitted from a source at position  $r = 0$  and time  $t = 0$  with amplitude  $A_0$  and pulse duration  $\tau_0$  disperses as it propagates to the sensor through the distance  $R$  and arrival time  $t_s$  with group velocity  $v_g$ . At the sensor, the ELF wave packet has amplitude  $A$  and pulse duration  $\tau$ . (b) Examples of ELF signal spectrograms with two possible central frequencies,  $\omega_0^{(1)}$  and  $\omega_0^{(2)}$ , and two possible delay times,  $\delta t_1$  and  $\delta t_2$ , with respect to the arrival of the GW/EM trigger. Dispersion leads to a frequency chirp  $d\omega/dt$  of the signal depending on the arrival time  $\delta t$  and the central frequency  $\omega_0$  [Eq. (8)].

For an ultrarelativistic field the characteristic energy of the ELF quanta  $\epsilon_0$  is dominated by the kinetic energy,  $\epsilon_0 = \hbar\omega_0 \approx \hbar ck_0$  (see Ref. [4] for details). By expanding the dispersion  $\omega(k)$  around  $k_0$  we identify the group velocity

$$\frac{v_g}{c} = \frac{1}{c} \left. \frac{\partial \omega}{\partial k} \right|_{k=k_0} = \frac{ck_0}{\omega_0} \approx 1 - \frac{1}{2} \left( \frac{mc^2}{\epsilon_0} \right)^2, \quad (3)$$

which leads to a delay of the arrival of the ELF pulse on Earth relative to the GW or EM trigger given by

$$\delta t = t_s - \frac{R}{c} = R \left( \frac{1}{v_g} - \frac{1}{c} \right) \approx \left( \frac{mc^2}{\epsilon_0} \right)^2 \frac{R}{2c}. \quad (4)$$

Thus a given delay time and central frequency can be associated with a particular ELF mass. The spread in group velocities is

$$\frac{\Delta v_g}{c} = \left( \frac{mc^2}{\epsilon_0} \right)^2 \frac{\Delta \epsilon}{\epsilon_0}, \quad (5)$$

where the energy spread from the source  $\Delta \epsilon = \hbar \Delta \omega = \hbar / \tau_0$  leads to a frequency spread  $\Delta \omega$ . Due to the dispersion, the duration of the pulse at the sensors on Earth is given by

$$\tau(t_s) = \sqrt{\tau_0^2 + \left( \frac{\Delta v_g t_s}{v_g} \right)^2} = \sqrt{\tau_0^2 + \left( \frac{2\Delta \epsilon \delta t}{\epsilon_0} \right)^2} = \sqrt{\tau_0^2 + \left( \frac{2\delta t}{\omega_0 \tau_0} \right)^2}. \quad (6)$$

In the limit when dispersion has significantly lengthened the pulse,  $\tau \gg \tau_0$ , Eq. (6) is approximated by

$$\tau \approx \frac{2\delta t}{\omega_0 \tau_0}, \quad (7)$$

which we call the ‘‘chirp approximation’’. This leads to a chirp of the frequency at the sensors on Earth, given by the derivative of the instantaneous frequency in Eq. (1):

$$\frac{d\omega(t)}{dt} = -\frac{\omega_0}{2\delta t}, \quad (8)$$

that depends only on the central frequency  $\omega_0$  and delay time  $\delta t$ .

### B. ELF detection with magnetometers

We consider both linear and quadratic interactions of the ELF  $\phi$  with our sensors:

$$\mathcal{L}^{(l)} = f_l^{-1} J^\mu \partial_\mu \phi, \quad (9)$$

$$\mathcal{L}^{(q)} = f_q^{-2} J^\mu \partial_\mu \phi^2, \quad (10)$$

where  $J^\mu = \bar{\psi} \gamma^\mu \gamma_5 \psi$  is the axial-vector current for Standard Model fermions and  $f_l$  and  $f_q$  are the characteristic energy scales of the linear and quadratic interactions, respectively. Transforming to a Hamiltonian representation, we arrive at the effective spin-dependent Hamiltonians

$$H^{(l)} \approx -\frac{2(\hbar c)^{3/2}}{f_l} \mathbf{S} \cdot \nabla \phi, \quad (11)$$

$$H^{(q)} \approx -\frac{2(\hbar c)^2}{f_q^2} \mathbf{S} \cdot \nabla \phi^2,$$

with  $\mathbf{S}$  being the atomic or nuclear spin [16]. The ELF can be treated as a so-called ‘‘pseudomagnetic field’’ since it causes energy shifts of Zeeman sublevels in a manner similar to the effect of a real magnetic field. To explicitly make the analogy between the Zeeman Hamiltonian ( $H_Z = -\boldsymbol{\mu} \cdot \mathbf{B}$ , where  $\boldsymbol{\mu} = \mu \mathbf{S}$  is the magnetic moment and  $\mathbf{B}$  is a magnetic field) and the Hamiltonians describing ELF-spin interactions, we introduce the corresponding pseudomagnetic fields:

$$\mathcal{B}_p^{(l)} = \frac{2(\hbar c)^{3/2}}{\mu_B f_l} \nabla \phi, \quad (12)$$

$$\mathcal{B}_p^{(q)} = \frac{2(\hbar c)^2}{\mu_B f_q^2} \nabla \phi^2,$$

where the Bohr magneton  $\mu_B$  is introduced as the unit of magnetic moment. To lowest order in  $1/R$ , one can show that the gradients of the waveform [Eq. (1)] at the detectors are:

$$\nabla \phi(R, t_s) \approx \frac{\hat{R}}{R} \sqrt{\frac{\Delta E}{2\pi^{3/2} c \tau}} \quad (13)$$

and

$$\nabla \phi^2(R, t_s) \approx \frac{\hat{R}}{R^2} \frac{\Delta E}{2\pi^{3/2} \omega_0 \tau}, \quad (14)$$

where  $\hat{R}$  is the unit vector pointing from the detector to the event location.

GNOME is designed to detect exotic spin interactions via the correspondence with the Zeeman interaction. For a given energy scale  $f^{l(q)}$ , the above considerations imply that an ELF incident on the GNOME network will manifest as a transient pseudomagnetic field  $\mathcal{B}_p$ . If the network has sufficient sensitivity, this will result in coincident detection of a pseudomagnetic field with the characteristic network pattern given by the orientations of different sensors. Alternatively, given a null detection, we can set limits on combinations of  $f^{l(q)}$  and the unknown initial energy release  $\Delta E$  via

$$f_l \times \left( \sqrt{\frac{1}{\Delta E}} \right) \gtrsim \frac{\hbar^{3/2} c}{\mu_B \mathcal{B}_p^* R} \sqrt{\frac{2}{\pi^{3/2} \tau}}, \quad (15)$$

$$f_q \times \left( \sqrt{\frac{1}{\Delta E}} \right) \gtrsim \frac{\hbar c}{R} \sqrt{\frac{1}{\pi^{3/2} \mu_B \mathcal{B}_p^* \omega_0 \tau}}, \quad (16)$$

where the pulse duration at the detector  $\tau$ , given by Eq. (6), is evaluated at the time of arrival of the ELF pulse  $t_s$  for a given  $\tau_0$ . The values of  $\Delta E$  and  $\tau_0$  can vary widely depending on the production theory [6, 8–11]. It is important to note that the observed frequency of the quadratic interaction corresponds to twice the central ELF frequency since the gradient of the field squared couples to the spin.

In the limit when significant dispersion has lengthened the ELF pulse,  $\tau$  can be evaluated with the chirp approximation [Eq. (7)] and the exclusion limits scale with the initial pulse duration by  $\tau_0^{1/2}$ . Without appreciable dispersion or lengthening of the pulse,  $\tau \approx \tau_0$ , the exclusion limits scale roughly as  $\tau_0^{-1/2}$ .

### III. GNOME NETWORK CHARACTERISTICS

GNOME comprises a global network of magnetically shielded alkali-atomic magnetometers [16–19]. These are located in over a dozen stations distributed over four continents. The sensors measure the projection of the ambient magnetic field on one sensitive axis via the variation of the Larmor spin precession of optically polarized alkali atoms in a vapor cell. Measurements are time-stamped using the Global Position System allowing for the use of coincident detection techniques to suppress unwanted background noises [19]. In addition, a multi-layer mu-metal magnetic shield, present in each station, suppresses background magnetic fields by a factor of  $\gtrsim 10^6$ . Because GNOME magnetometers use atoms whose nuclei have a valence proton, they are sensitive to proton-spin couplings with the ELF. The expected ELF signal amplitudes measured by the sensors will be proportional to the relative contribution of the proton spin to the nuclear spin [19]. ELFs can also couple to electron spins but the signal is attenuated by the electrons in the magnetic shields. To first order it was expected this attenuation is the same as the magnetic shielding factor [20] but the orbital angular momentum of the electrons in the shields can lessen this effect [21]. The coupling to electron spins is ignored in this manuscript.

In Table I, we present some characteristics of the sensors in the network. More detailed descriptions of the sensors and the network are given in Ref. [18]. For this work, each sensor has bandwidth of approximately 100 Hz. The

Station	Location		Orientation		$\sigma/g_f$
	Longitude	Latitude	Az	Alt	
Beersheba	34.8043° E	31.2612° N	180°	0°	0.50 <sup>+0.00</sup> <sub>-0.19</sub>
Beijing	116.1868° E	40.2457° N	251°	0°	-0.39 <sup>+0.19</sup> <sub>-0.00</sub>
Berkeley	122.2570° W	37.8723° N	0°	90°	-0.39 <sup>+0.19</sup> <sub>-0.00</sub>
Canberra	149.1185° E	35.2745° S	0°	90°	0.70 <sup>+0.00</sup> <sub>-0.15</sub>
Daejeon	127.3987° E	36.3909° N	0°	90°	-0.39 <sup>+0.19</sup> <sub>-0.00</sub>
Hayward*	122.0539° W	37.6564° N	0°	90°	0.70 <sup>+0.00</sup> <sub>-0.15</sub>
Hefei	117.2526° E	31.8429° N	90°	0°	-0.38 <sup>+0.05</sup> <sub>-0.00</sub>
Krakow	19.9048° E	50.0289° N	45°	0°	0.50 <sup>+0.00</sup> <sub>-0.11</sub>
Lewisburg*	76.8825° W	40.9557° N	0°	90°	0.70 <sup>+0.00</sup> <sub>-0.15</sub>
Los Angeles*	118.4407° W	34.0705° N	270°	0°	0.50 <sup>+0.00</sup> <sub>-0.07</sub>
Mainz	8.2354° E	49.9915° N	0°	-90°	0.50 <sup>+0.00</sup> <sub>-0.11</sub>
Moxa*†	11.6147° E	50.6450° N	270°	0°	-0.39 <sup>+0.19</sup> <sub>-0.00</sub>
Oberlin*	81.7796° W	41.2950° N	276°	0°	-0.49 <sup>+0.18</sup> <sub>-0.00</sub>

TABLE I. Location, orientation and proton spin couplings of sensors in GNOME. \* marking denotes the stations that were active with quality data during the S200311bg event. (†Moved from Fribourg to Moxa in 2018.)

response and sensitivity of each sensor is determined by calibration signals at multiple frequencies. Magnetic-field measurements are recorded at a sampling rate of 512 samples per second. In addition, a 1 sample per second data glitch / data quality indicator is also written to file. This boolean variable is derived from auxiliary sensors which monitor temperature, accelerations, magnetic field outside the shielding, rotation and other user-defined variables

such as laser intensity, frequency, etc. If any of those quantities vary outside an allowed range within a given second, the data-quality flag – which is normally true – is switched to false. In our analysis, we disregard all the data having data quality flag false.

While an incident ELF yields a common pseudomagnetic field  $\mathcal{B}_p$ , each particular sensor, denoted throughout with a superscript  $i$ , will sense an effective magnetic field  $B^i$ , which is proportional to the projection of  $\mathcal{B}_p$  on the sensor's sensitive axis  $\hat{m}^i \cdot \hat{R}$  and the ratio between the proton-spin coupling and the Landé  $g$ -factor  $g_F$  ( $\sigma^i/g_F^i$ ) [19]. Thus a field  $\mathcal{B}_p$  incident on the network results in data values  $d_i(t)$  from a sensor  $i$  of the form

$$d^i(t) = B^i(t) + n^i(t), \quad (17)$$

where

$$B^i(t) = \frac{\sigma^i \hat{m}^i(t) \cdot \hat{R}}{g_F^i} \mathcal{B}_p(t) \quad (18)$$

is the contribution of the signal from the ELF, and  $n_i(t)$  represents the environmental and sensor noise. We have assumed above that the detector bandwidths are much greater than the frequency spread of the signal. Astrophysical observations provide the distance  $R$  of the event as well as the direction  $\hat{R}$  given by right ascension and declination coordinates.

Because we are searching for an ELF signal with a mass-dependent central frequency and delay time, our analysis uses spectrograms formed by taking discrete Fourier transforms of subsets of the time series  $d^i(t)$ . The output of the spectrogram is divided into “tiles” of the time-frequency plane. We reserve the subscript  $j$  for a tile's central time coordinate and the subscript  $k$  for the central frequency coordinate. The tile amplitudes are thus related to the time-domain signals via

$$\tilde{d}_{jk}^i = \tilde{B}_{jk}^i + \tilde{n}_{jk}^i, \quad (19)$$

where  $\tilde{B}_{jk}^i$  and  $\tilde{n}_{jk}^i$  are the Fourier transform amplitudes at frequency index  $k$  for a time subset denoted by  $j$ , and include the effects of the finite bandwidths of the detectors. Therefore, for each tile the form of an ELF signal at sensor  $i$  is given by:

$$\tilde{B}_{jk}^i = \frac{\sigma^i \hat{m}_j^i \cdot \hat{R}}{g_F^i} \beta_k^i \tilde{\mathcal{B}}_{p,jk}, \quad (20)$$

which has the same form as the equivalent expression in the time domain [Eq. (18)].  $\tilde{\mathcal{B}}_{p,jk}$  represents the amplitude of  $\mathcal{B}_p$  in the frequency band associated with index  $k$  and time  $j$ .  $\beta_k^i$  are transfer functions accounting for the response at frequency  $k$  of sensor  $i$  and are measured by applying magnetic fields of known frequency and amplitude. Figure 2 displays an example of the projection of the ELF gradient on the sensitive axes of the magnetometers. The color maps are the individual station's scaling between  $\mathcal{B}_p$  and  $B^i$  [Eq. (20)] over the time-frequency space that is searched in this paper.

For our analysis, we use spectrogram tiles of area  $\Delta f \times \Delta t = 1$ . As we discuss in Sec. IV A, the aspect ratio of these tiles is adapted to match the expected characteristics of a signal at a specific delay time and frequency.

#### IV. ELF ANALYSIS PIPELINE

Our analysis focuses on a search for a signal recorded with GNOME that is coincident with an observation of an astrophysical event and consistent with the signal-propagation model described in Sec. II. Figure 3 illustrates how data from the network are sent through the analysis pipeline – leading to either the detection of ELF candidates or the determination of upper limits. The pipeline steps are:

- **Spectrogram:** Spectrograms of the time-series data from the network characterize the data in the time-frequency plane. The optimal temporal and frequency resolution is set by the arrival time of the GW/EM trigger and the expected-signal model. We tile the time-frequency plane adaptively to match the modeled signal characteristics as described in more detail in Sec. IV A.
- **Excess power (EP) cut:** For the first stage of the analysis, we perform a model agnostic EP cut [22] on the spectrograms to identify network-wide, relatively high power tiles labelled by their time-frequency coordinates. We apply a threshold on the joint EP probability of coincident tiles  $\zeta^\epsilon$ . This serves primarily to reduce the amount of data needing further analysis. We discuss this further in Sec. IV B.



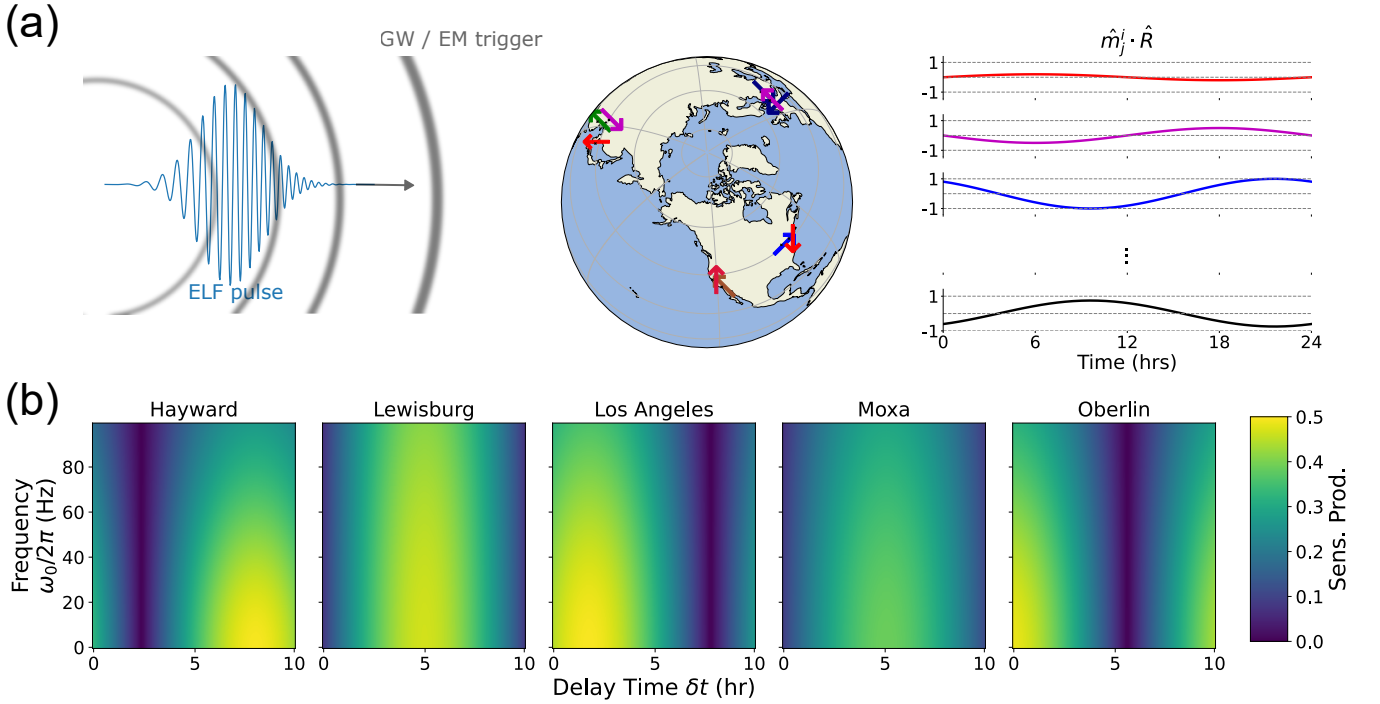


FIG. 2. (a) Cartoon picture of the GNOME network with arrows representing GNOME detectors and their sensitive axes. The arrival of a GW/EM trigger heralds the ELF pulse. The projection of the ELF on detector axes is modulated by Earth's rotation. (b) Sensitivity product for each station which is the product of the directional sensitivity  $\hat{m}_j^i \cdot \hat{R}$ , frequency response  $\beta_k^i$ , and ratio of proton-spin coupling and the Lande g-factor  $\sigma^i/g_F^i$  [Eq. (20)] across the foreground window for the BBH merger search target considered. We update the directional sensitivity at one minute intervals and the frequency response at 1 Hz intervals.

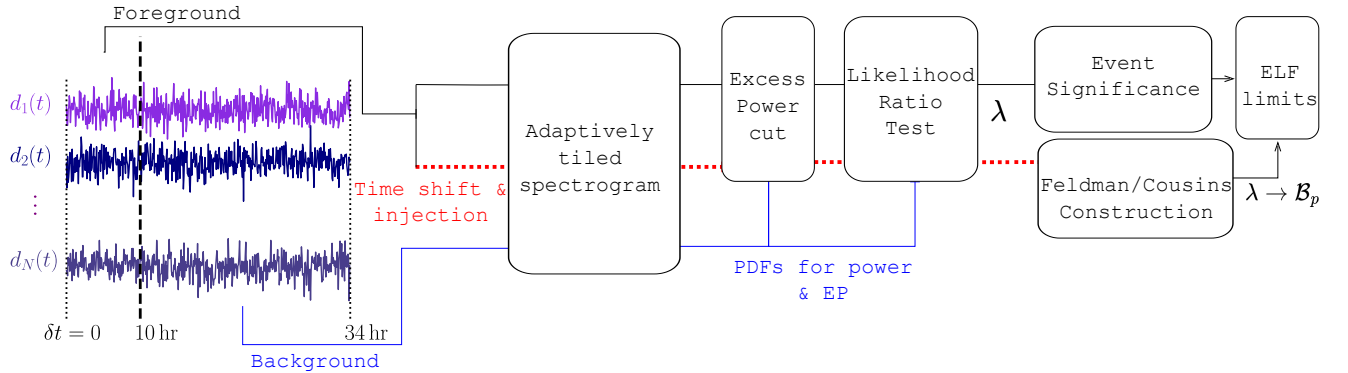


FIG. 3. Flowchart illustrating the analysis pipeline. A search is triggered by some GW or EM observation. Time-series measurements from the network in the foreground and background windows are represented in the time-frequency plane by spectrograms with tile dimensions chosen to match the ELF chirp rate. The EP cut passes network-wide, relatively high power tiles to the next stage as candidate tiles. The LRT statistic  $\lambda$  is determined for each candidate tile and is compared to a signal-free distribution of  $\lambda$  to determine the significance. The test statistic is translated to a pseudomagnetic amplitude  $\mathcal{B}_p$  with the Feldman-Cousins construction and ELF limits are calculated.

- **Likelihood-ratio test (LRT):** Next, we perform a general LRT on the coincident tiles that passed the first stage [23]. We fit the data to determine the most likely ELF pseudomagnetic field  $\mathcal{B}_p$  and produce a test statistic  $\lambda$  that quantifies the likelihood of an ELF signal + noise hypothesis against a noise-only hypothesis. We time-shift the data to effectively generate a large number of noise-only datasets which are used to determine the expected distributions of the test statistic. We discuss this further in Sec. IV C.
- **Confidence-belt construction:** To characterize the network sensitivity across the time-frequency space, we

determine confidence belts using the Feldman-Cousins (FC) construction [24]. We inject ELF signals with amplitude  $\mathcal{B}_p$  into time-shifted data at coarse times and frequencies and perform the LRT to determine distributions of  $\lambda$  in the presence of a signal. These confidence belts form a mapping between the test statistic  $\lambda$  and the ELF pseudomagnetic field  $\mathcal{B}_p$ . We discuss this further in Sec. IV D.

- **Event significance:** We determine the false positive probability of each candidate tile using the time-shifted distributions of the test statistic. We discuss this further in Sec. IV E.
- **ELF detection or limits:** If a tile with a significant test statistic is found the FC construction is used to translate this into a confidence belt on the ELF amplitude  $\mathcal{B}_p$ . If no significant tiles are detected, we place an upper limit on the test statistic in each box by requiring the total false probability rate to be less than one over our dataset. We translate these to upper limits on the ELF amplitude via the FC construction. We then place limits on the combination of ELF couplings, the initial ELF-pulse duration, and energy release via the quantities  $f_l\sqrt{1/\Delta E}$  and  $f_q\sqrt{1/\Delta E}$  [Eqs. (15)-(16)]. Section V details our determination of ELF parameter upper limits.

### A. Spectrograms with adaptive tiling

In time-frequency analysis methods, there is an inherent trade-off in localization in the time and frequency domains [25]. The tiling resolution for optimal signal-to-noise ratio is that which best matches the temporal and frequency spread of the signal and underlies methods such as wavelets and Q-transforms [26, 27]. While we do not a priori know the duration of the ELF signal or its frequency spread, we do know that a signal arriving at a delay time and frequency coordinate  $\{\delta t, \omega_0\}$  will be chirped at a rate  $d\omega/dt \approx -\omega_0/2\delta t$  [Eq. (8)]. This suggests that the spectrogram tile dimensions should have the ratio

$$\frac{\Delta\omega}{\Delta t} \approx \frac{\omega_0}{2\delta t}. \quad (21)$$

Combining this constraint with the tile area given by the discrete Fourier transform,  $\Delta\omega\Delta t = 2\pi$ , gives unique tile dimensions over the delay time-frequency plane, which motivates our use of adaptive tiling.

We divide the foreground window into “boxes” that span regions of delay time and frequency as shown in Fig. 4. For each box, we use tile dimensions, denoted by the box color, to approximate the ratio given by Eq. (21). Power spectrograms with the denoted tile dimensions are calculated in each box, giving the powers of individual tiles

$$P_{jk}^i = \left| \tilde{d}_{jk}^i \right|^2, \quad (22)$$

where  $\tilde{d}$  are the amplitudes defined in Eq. (19) with  $i$  denoting the sensor,  $j$  the delay time, and  $k$  the frequency. We do not consider the DC band as the ELF signal is an oscillating transient.

The discussion above applies when the ELF wave packet has dispersed as it propagates to Earth, i.e.  $\tau \gg \tau_0$ . As discussed in Sec. II A, this occurs when  $2\delta t/\omega_0\tau_0 \gg \tau_0$ . For the shortest delay times and highest frequencies this chirp approximation does not hold. Here we do not apply any adaptive tiling and use the smallest tile dimension of  $1\text{ s} \times 1\text{ Hz}$ .

### B. Excess power cut

The next step in our analysis is a cut based on EP. Excess power is a model-agnostic test statistic used to identify tiles that have power greater than the average noise [28]. Although less powerful than matched filtering, it provides an optimal search method for signals of unknown form [22]. In our analysis, a cut on the EP is performed primarily to reduce the amount of data to be processed by the model-dependent LRT.

With our adaptive tiling, the tile dimension depends on which box is being analyzed. Below, we focus on the analysis for a single tile dimension. First, the unitless EP statistic  $\varepsilon_{jk}^i$  for a tile of sensor  $i$ , at time  $j$ , and frequency  $k$  is determined

$$\varepsilon_{jk}^i = P_{jk}^i / \bar{P}_k^i, \quad (23)$$

where the measured power  $P_{jk}^i$  is normalized by the average power  $\bar{P}_k^i$  over the entire dataset for the respective frequency  $k$ . Figure 5 displays a contrast of the measured power and EP in a single time-frequency box for a single station.



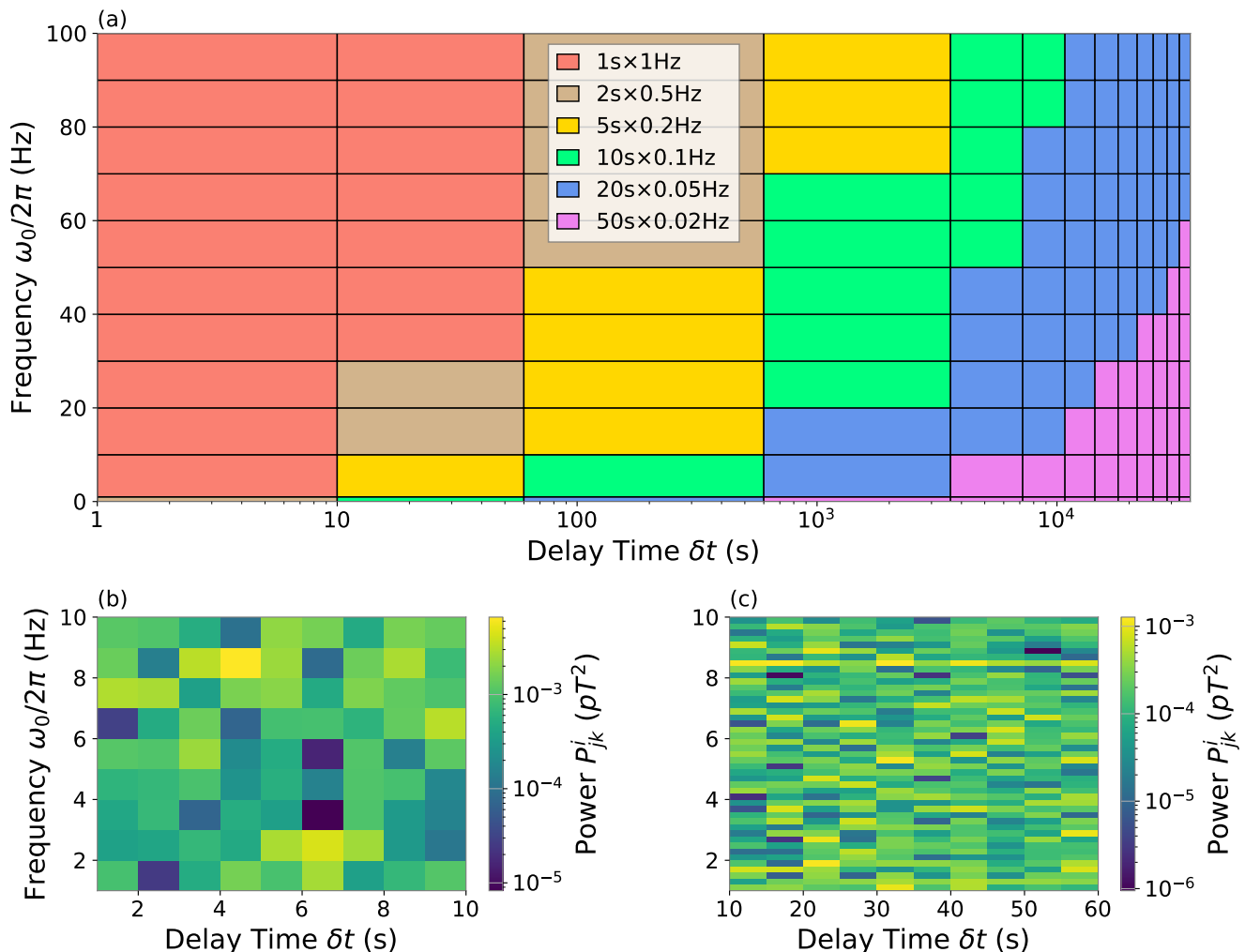


FIG. 4. (a) Map of the adaptive tiling used to match the spectrogram tile dimensions to the chirp rate. The searched time-frequency space (foreground window),  $\delta t \in [0, 10]$  hr  $\times$   $f_0 \in [0, 100]$  Hz, is partitioned into “boxes” with boundaries marked by black lines. The box color indicates the tile dimension used that approximates the chirp rate given by Eq. (8). (b) Spectrogram of Lewisburg data with tile dimension  $1 \text{ s} \times 1 \text{ Hz}$  contained within the box spanning  $f_0 \in [1, 10]$  Hz and  $\delta t \in [1, 10]$  s. The relative color of each tile represents the measured power in the tile. (c) Spectrogram of Lewisburg data with tile dimension  $5 \text{ s} \times 0.2 \text{ Hz}$  contained within the box adjacent to (b) spanning  $f_0 \in [1, 10]$  Hz and  $\delta t \in [10, 60]$  s.

In the presence of pure Gaussian noise, EP would be a chi-squared distributed statistic with two degrees of freedom. Our data, however, empirically deviates from this simple exponential, particularly in the tails of the probability density function (PDF), due to unique noise present in certain sensors. To avoid assumptions about Gaussianity when comparing stations, we construct empirical PDFs  $f^i(\varepsilon)$  for each station. The empirical PDFs are formed using data from a background window consisting of the following 24 hours and are frequency-independent.

To form the empirical PDFs, we histogram the background power data with bin widths that monotonically increase as the probability density decreases. The width of the bin for the highest power, which serves as a conservative estimate of the probability density for rare tiles, is set to contain the largest of either the maximum background or foreground tile. We use the empirical PDF as a look-up table to estimate the probability densities  $\rho_{jk}^i = f^i(\varepsilon_{jk}^i)$ , for every tile. Figure 6 depicts PDFs constructed for this search to illustrate the difference between stations.

The joint probability density in each tile is found by taking a product of all  $N$  active stations’ PDFs at each tile

$$\zeta_{jk} = \prod_{i=1}^N \rho_{jk}^i. \quad (24)$$

A coincidence threshold  $\zeta_{th}$  is determined for each tile size that would pass the loudest (least likely) 1% of background

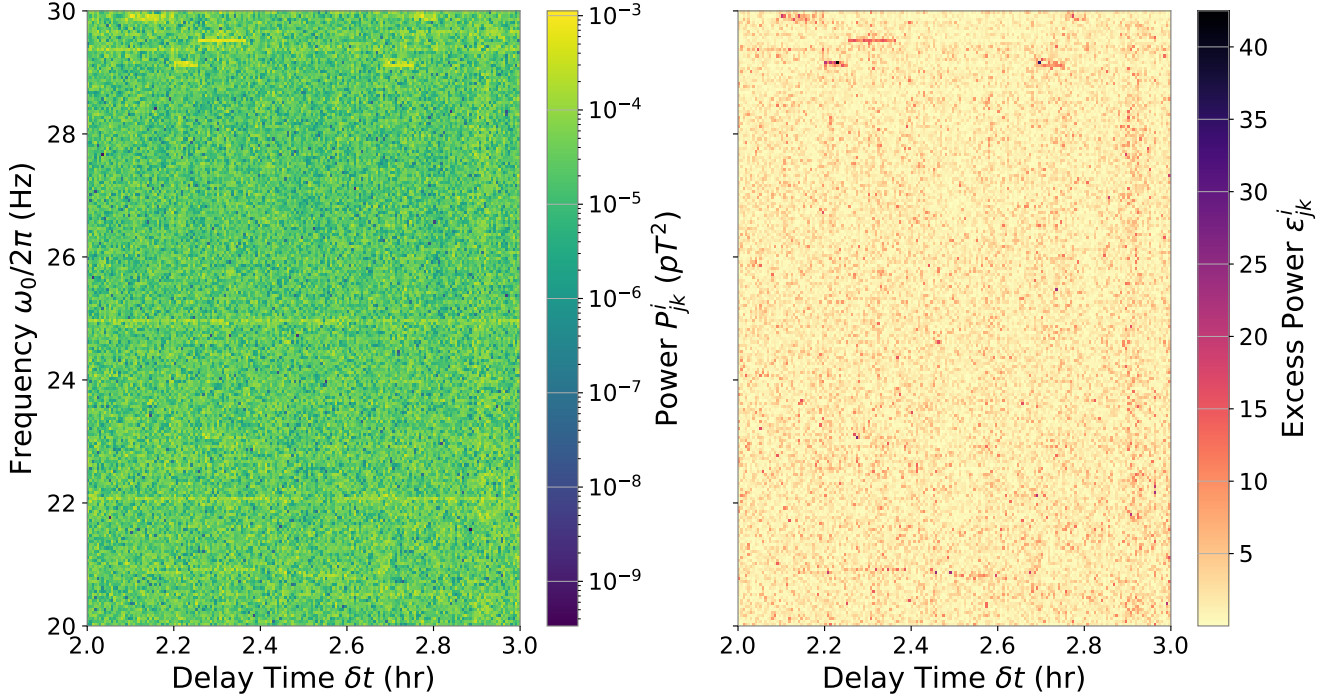


FIG. 5. Whitening of spectrogram of  $P_{jk}^i$  and corresponding EP statistic  $\varepsilon_{jk}^i$  of Lewisburg data [Eq. (23)]. The relative color of each tile in each plot represents the measured power (on the left) and EP (on the right) in the tile. Note that the constant higher power bands at 22 Hz and 25 Hz are “whitened” to average EP values. The loud spikes in the 29 Hz–30 Hz range are mellowed due to their repetition while the quiet regions are especially suppressed due to the larger average noise. The features in the 29 Hz–30 Hz range indicate non-stationarity which is not suppressed by taking the EP.

tiles. Tiles with joint probability  $\zeta_{jk}$  lower than the threshold are passed to the next part of the analysis.

### C. Likelihood-ratio test

We next employ a LRT to quantify whether candidate tiles are best described by a noise-only or a signal-plus-noise hypothesis. Below, we describe this process for a set of tiles with a single tile dimension. The same procedure is repeated for each tile dimension.

First, we characterize the noise behavior of the stations in the absence of a signal. We construct noise log-PDFs  $g_k^i(P)$  of the observed power for each station  $i$  at each frequency  $k$  from the 24-hour background window. Similar to EP PDFs, we build the noise log-PDFs by interpolating the log of a normalized histogram of the background powers at each frequency, with varying bin widths that contain at least one tile per bin. The tails of the noise log-PDFs are modelled with a linear extrapolation using the background data with the 5% highest power. Figure 7 is an example of a log-PDF constructed for a particular station, tile dimension, and frequency.

The noise log-PDFs  $g_k^i(P)$  give the log of the relative probability of detecting a power  $P$  in the absence of a signal, i.e. no ELF pseudomagnetic field  $\mathcal{B}_p = 0$ . In other words, they are the log-likelihood functions  $\ell_i(\mathcal{B}_p = 0|P) = g_k^i(P)$  for the noise-only hypothesis of a single station given an observed power  $P$ .

For the signal hypothesis ( $\mathcal{B}_p \neq 0$ ), we will vary  $\mathcal{B}_p$  to find the maximum log-likelihood value, similar to a least squares fit. The log-likelihood is determined by evaluating the noise log-PDFs at the residual power  $\eta_{jk}^i(\mathcal{B}_p)$  given by

$$\eta_{jk}^i(\mathcal{B}_p) \equiv \left[ \left| \tilde{d}_{jk}^i \right| - \left| \tilde{B}_{jk}^i(\mathcal{B}_p) \right| \right]^2 = \left[ \sqrt{P_{jk}^i} - \left| \tilde{B}_{jk}^i(\mathcal{B}_p) \right| \right]^2, \quad (25)$$

where  $\tilde{d}_{jk}^i$  is observed signal amplitude,  $\tilde{B}_{jk}^i(\mathcal{B}_p)$  is the expected signal amplitude for ELF pseudomagnetic field  $\mathcal{B}_p$  [Eq. (20)], and  $P_{jk}^i$  is the observed power for station  $i$ . Absolute values are used since the frequency-dependent phase responses of the individual stations were not calibrated and are unknown. Note that in the absence of a signal the residual is just the observed power,  $\eta_{jk}^i(\mathcal{B}_p = 0) = P_{jk}^i$ .

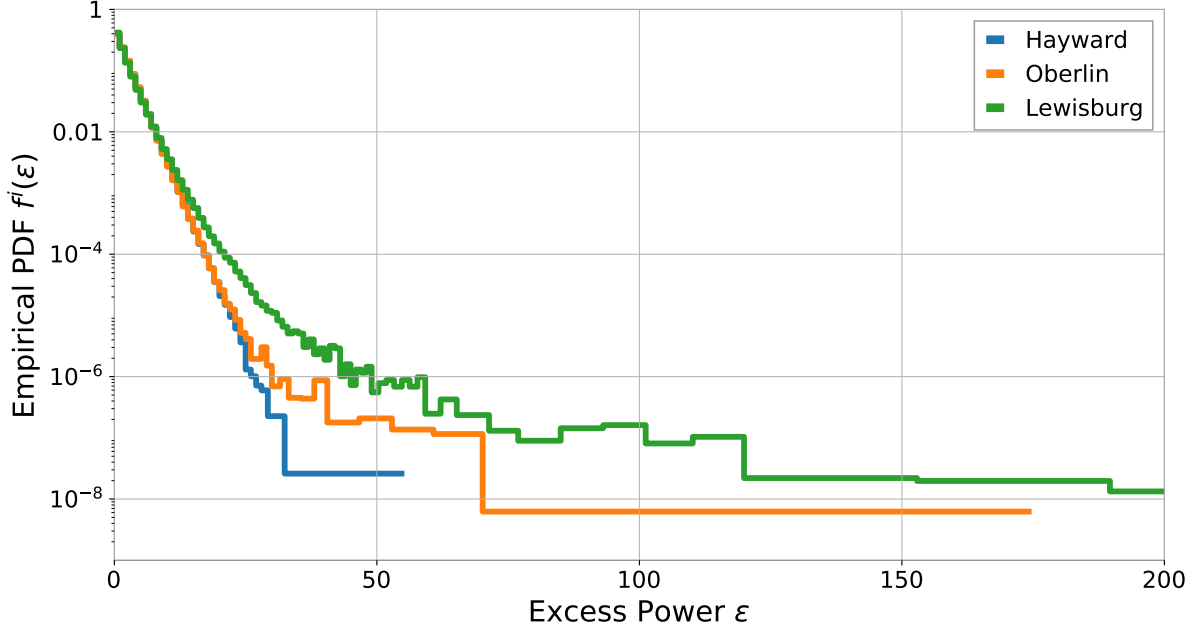


FIG. 6. Empirical EP PDFs  $f^i(\varepsilon)$  of three stations with tile dimension  $5\text{ s} \times 0.2\text{ Hz}$ . The PDFs serve as a look-up table to convert the EP statistic  $\varepsilon$  to a probability density  $\rho$ . The significantly differing behavior at large  $\varepsilon$  highlights the need to construct empirical PDFs to compare stations.

The total log-likelihood  $\ell$  for a hypothesis of a signal size  $\mathcal{B}_p$ , given a set of observed powers at each station  $\vec{P}_{jk} \ni P_{jk}^i$ , is then given by the sum of the station log-likelihoods

$$\ell(\mathcal{B}_p|\vec{P}_{jk}) = \sum_{i=1}^N g_k^i [\eta_{jk}^i(\mathcal{B}_p)]. \quad (26)$$

We fit our observed data by varying the ELF pseudomagnetic field  $\mathcal{B}_p$  to maximize the log-likelihood  $\ell(\mathcal{B}_p|\vec{P})$ .

Finally, the likelihood-ratio test statistic  $\lambda$  is typically defined to be twice the log of the ratio of the maximum likelihood for the signal hypothesis to the likelihood of the noise-only hypothesis. Because we use log-likelihoods this is simply given by the difference:

$$\lambda_{jk} = 2 \left[ \max_{\mathcal{B}_p > 0} \ell(\mathcal{B}_p|\vec{P}_{jk}) - \ell(\mathcal{B}_p = 0|\vec{P}_{jk}) \right], \quad (27)$$

where a larger value of  $\lambda$  means the signal hypothesis is more likely.

This procedure determines a test statistic for each candidate tile. However, to determine the statistical significance of a candidate tile, we need to compare the same analysis performed on signal-free data. This signal-free data is generated by “time-shifting” data in the foreground window, i.e. choosing a set of tiles with random times for each station. After passing the time-shifted data through the EP cut, the same LRT is performed to generate test statistics in the absence of a signal.

#### D. Feldman-Cousins confidence belts

We build FC confidence belts [24] to determine a confidence interval or an upper limit on the pseudomagnetic ELF amplitude  $\mathcal{B}_p$  for a given LRT statistic  $\lambda$ . The confidence belts are formed from the distributions of  $\lambda$  determined from LRTs with signals of different amplitudes  $\mathcal{B}_p$  injected into time-shifted foreground data. For  $\mathcal{B}_p = 0$ , we use the

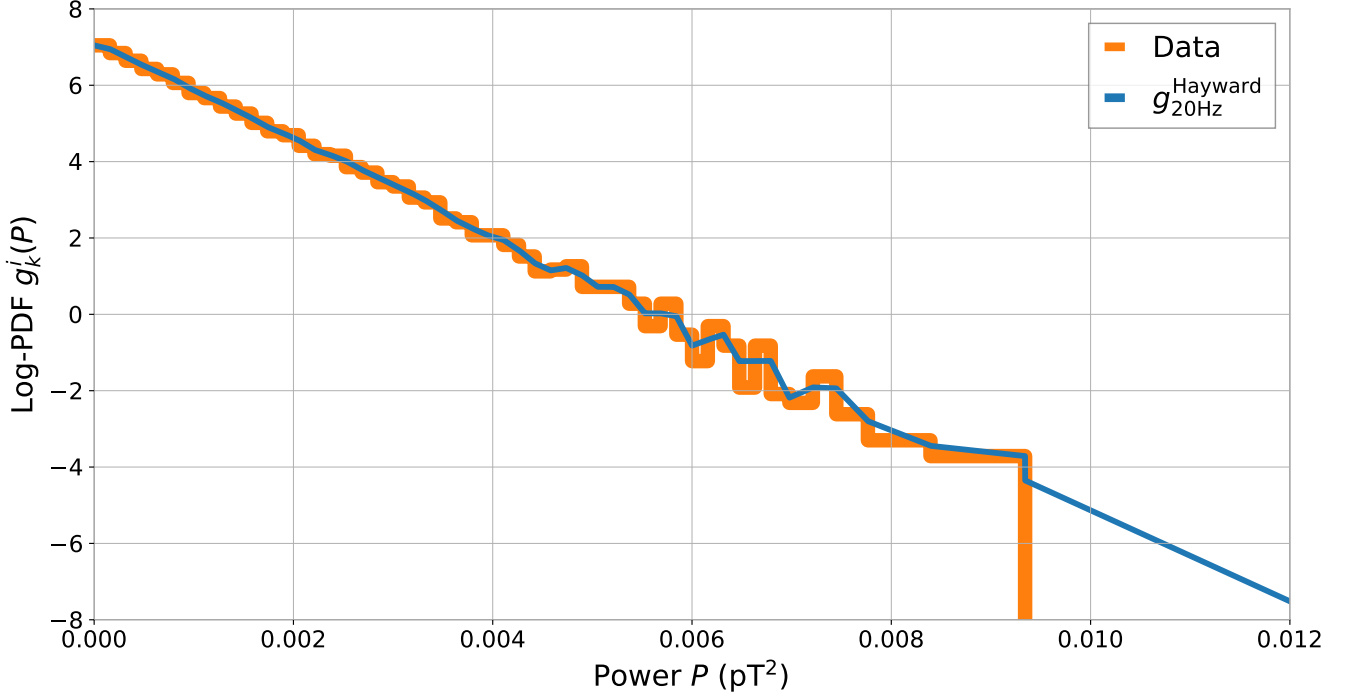


FIG. 7. Example of the construction of a noise log-PDF  $g_k^i(P)$  from binned data with interpolation and linear extrapolation. Shown is the Hayward station at 20Hz for the tile dimension  $2\text{ s} \times 0.5\text{ Hz}$ .  $g_k^i(P)$  are constructed for every unique choice of station, tile dimension, and frequency.

same distributions from the previous section that were determined from the randomly time-shifted data. As described in Eq. (1), the signal model is a sine-Gaussian chirp and we inject signals of the form

$$\psi^i(t) = B^i(t|\mathcal{B}_p)e^{-4 \ln 2 \frac{t^2}{\Delta t^2}} \cos \left[ \left( \omega_0 - \frac{\Delta \omega}{2\Delta t} t \right) t \right]. \quad (28)$$

The observed amplitude  $B^i(t|\mathcal{B}_p)$  for station  $i$  is determined from  $\mathcal{B}_p$  and the station sensitivity as described by Eq. (18). The chirp rate  $\Delta \omega / \Delta t$  is chosen with Eq. (21) for each box in Fig. 4. The Gaussian envelope is set to have a full-width half-maximum equal to the tile dimension  $\Delta t$ . We inject 1000 chirps for each amplitude  $\mathcal{B}_p$  and after performing LRT, we use the resulting distributions of the test statistic  $\lambda$  to form the confidence belts in the FC plot as shown in Fig. 8. We construct a FC plot for every time-frequency box in Fig. 4.

For a candidate tile, a confidence interval for the pseudomagnetic field  $\mathcal{B}_p$  can be determined from the intersection of a vertical line at the tile's  $\lambda$  with the confidence belts. If there are no statistically significant tiles in a box the FC belts are used to place an upper limit on  $\mathcal{B}_p$ .

### E. Event significance

To determine the significance of a candidate tile, we first calculate the false positive ratio (FPR), which we define as the number of candidate tiles above a threshold test statistic in a signal-free dataset per total candidate tiles. The FPR in the  $n$ th box (see Fig. 4) for a given threshold value  $\lambda^{th}$  is related to the Cumulative Distribution Function  $\text{CDF}_n^\lambda$  of the  $\lambda$  values of the time-shifted data in box  $n$  by

$$\text{FPR}_n(\lambda^{th}) = \frac{\text{tiles in box } n \text{ of time-shifted data with } \lambda > \lambda^{th}}{\text{tiles in box } n \text{ of time-shifted data}} = 1 - \text{CDF}_n^\lambda(\lambda = \lambda^{th}). \quad (29)$$

Using many time-shifts allows an estimate of the  $\text{FPR}_n$  even for signal thresholds higher than those observed in the foreground.

The FPR of a candidate tile can then be used to calculate the expected mean number of false positives  $\mu$  in a dataset. For the foreground data

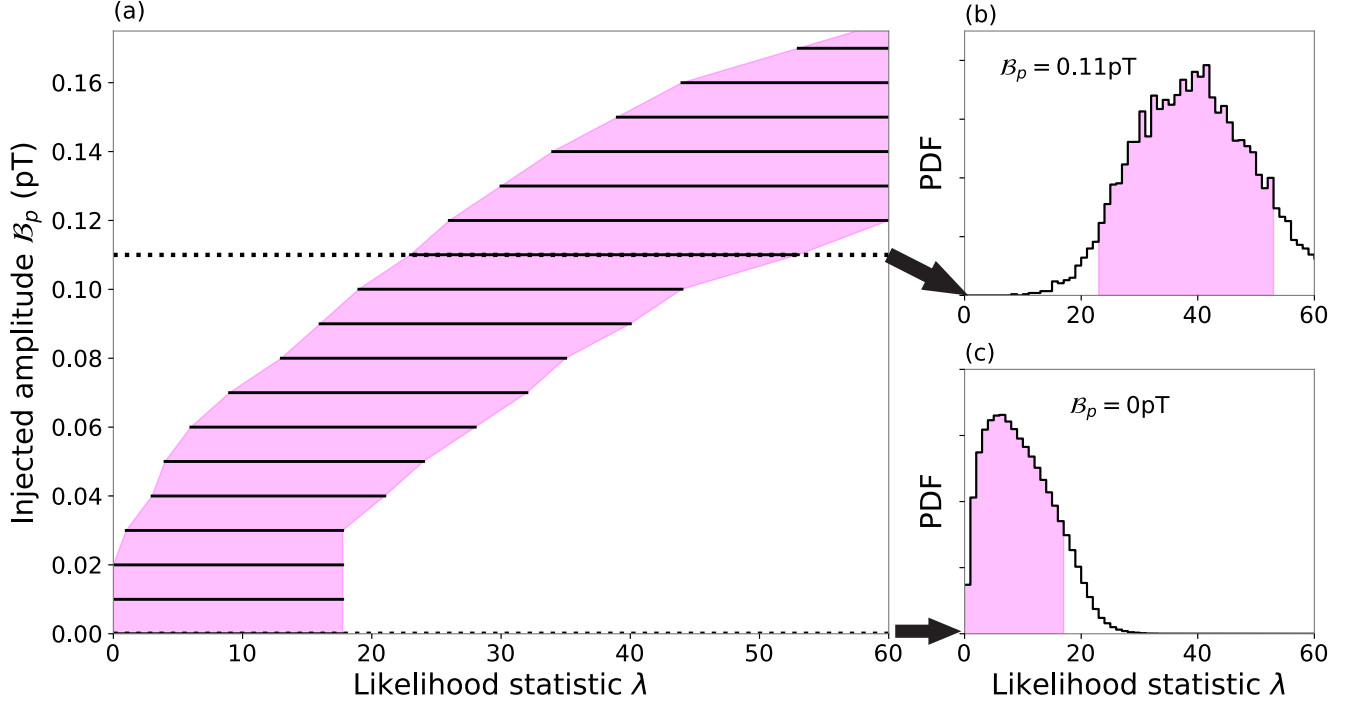


FIG. 8. (a) FC plot used to translate  $\lambda$  to  $B_p$  in the time-frequency box (see Fig. 4) spanning  $f_0 \in [30,40]$  Hz and  $\delta t \in [3600,7200]$  s with tile dimension  $20 \text{ s} \times 0.05 \text{ Hz}$ . (b) The distribution of  $\lambda$  with injected signals of  $B_p = 0.11$  pT. Shading represents the 90% acceptance interval from the FC construction that constitutes the horizontal belt. (c) The signal-free distribution of  $\lambda$  at  $B_p = 0$  from time-shifted data.

$$\mu_n(\lambda) = \text{FPR}_n(\lambda) \times N_n^{fg}, \quad (30)$$

where  $N_n^{fg}$  is the number of foreground tiles in box  $n$ . For  $\mu \ll 1$ , the false positive probability (FPP), i.e. the probability to observe one or more false positives, is approximately the mean value<sup>1</sup>,

$$\text{FPP}_n(\lambda) \approx \mu_n(\lambda) = \text{FPR}_n(\lambda) \times N_n^{fg}. \quad (31)$$

Across the entire dataset the  $\text{FPP}_{tot}$  for a given FPR is then

$$\text{FPP}_{tot} \approx \mu_{tot} = \text{FPR}_n(\lambda) \times N_{tot}^{fg}, \quad (32)$$

where  $N_{tot}^{fg}$  is the total number of all foreground tiles.

Using the total number of tiles is equivalent to correcting for the “look-elsewhere” effect with a trials factor of  $N_{tot}^{fg}/N_n^{fg}$  [29]. If the foreground tiles were evenly distributed amongst the boxes (which in our case have very different areas in time-frequency space), this trials factor would be equal to the number of boxes.

The significance of an event detection can be evaluated from its FPP. For example, a  $3\sigma$  detection corresponds to a FPP of  $2.7 \times 10^{-3}$ . If no significant events are detected, we determine a threshold test statistic for each box such that  $\mu_{tot} \leq 1$  for our entire foreground dataset.

In either case, the FC belts can be used to translate the test statistic into a pseudomagnetic field which can then be converted to a combination of the possible ELF energy scales  $f^{l(q)}$ , initial energy release  $\Delta E$ , and initial pulse duration  $\tau_0$  as described in Sec. II B.

<sup>1</sup> The probability of getting  $k$  events for a Poissonian process with a mean value  $\mu$  over an observation window is  $\Pr(k) = \mu^k e^{-\mu} / k!$ . For rare events, the probability of getting one or more events in the limit of  $\mu \ll 1$  is  $\Pr(k \geq 1) = 1 - \Pr(k = 0) \approx 1 - e^{-\mu} \approx \mu$ .

## V. SEARCH TARGET AND RESULTS

We now apply this analysis method to the BBH merger S200311bg (denoted as GW200311\_115853 in Ref. [30]) detected by LIGO/Virgo on March 11th, 2020 at 11:58:53.398 UTC [14, 30]. The luminosity distance is estimated to be  $D_L = 1.17^{+0.28}_{-0.40}$  Gpc at right ascension 00h08m and declination -07d27m with a sky localization of  $35 \text{ deg}^2$ . The total mass before the merger was  $61.9^{+5.3}_{-4.2} M_\odot$  and the final mass was  $59.0^{+4.8}_{-3.9} M_\odot$ .

### A. Foreground analysis

GNOME had 5 active stations with quality data at the time of and after the merger that are used in this analysis: Hayward, Lewisburg, Los Angeles, Moxa, and Oberlin. The 10-hour foreground window searched by the analysis is from March 11th, 2020 at 11:58:53 UTC to 21:58:53 UTC and the 24-hour background window is from March 11th, 2020 at 21:58:53 UTC to March 12th, 2020 at 21:58:53 UTC. The background window was taken after the foreground window to maximize the available data from the 5 active stations.

Figure 9 shows the cumulative number of foreground events above a given FPP versus the mean number of expected events. The foreground and time-shifted data are largely consistent. The most significant event had an expected mean of  $\mu_{tot} = 0.23$  or FPP= 0.21, which would correspond to a detection with a significance of only  $1.3\sigma$ . While this is not significant, we calculate the corresponding ELF masses and energy scales as an example. This tile occurred at a delay time of 15920s and a central frequency of 95.8 Hz. Through the FC method, we obtain a 90%-confidence upper limit of  $\mathcal{B}_p < 0.08 \text{ pT}$ . For the linear interaction, this corresponds to a mass of  $m = 2.1 \times 10^{-19} \text{ eV}$  [Eq. (33)] and linear energy scale of  $f_l = 87.4 \text{ GeV}$  at  $\tau_0 = 1 \text{ s}$  and  $\Delta E = 1 M_\odot c^2$  [Eq. (15)]. For the quadratic interaction, the mass is  $m = 1.0 \times 10^{-19} \text{ eV}$  and the quadratic energy scale is  $f_q = 0.2 \text{ GeV}$  at  $\tau_0 = 1 \text{ s}$  and  $\Delta E = 1 M_\odot c^2$  [Eq. (16)].

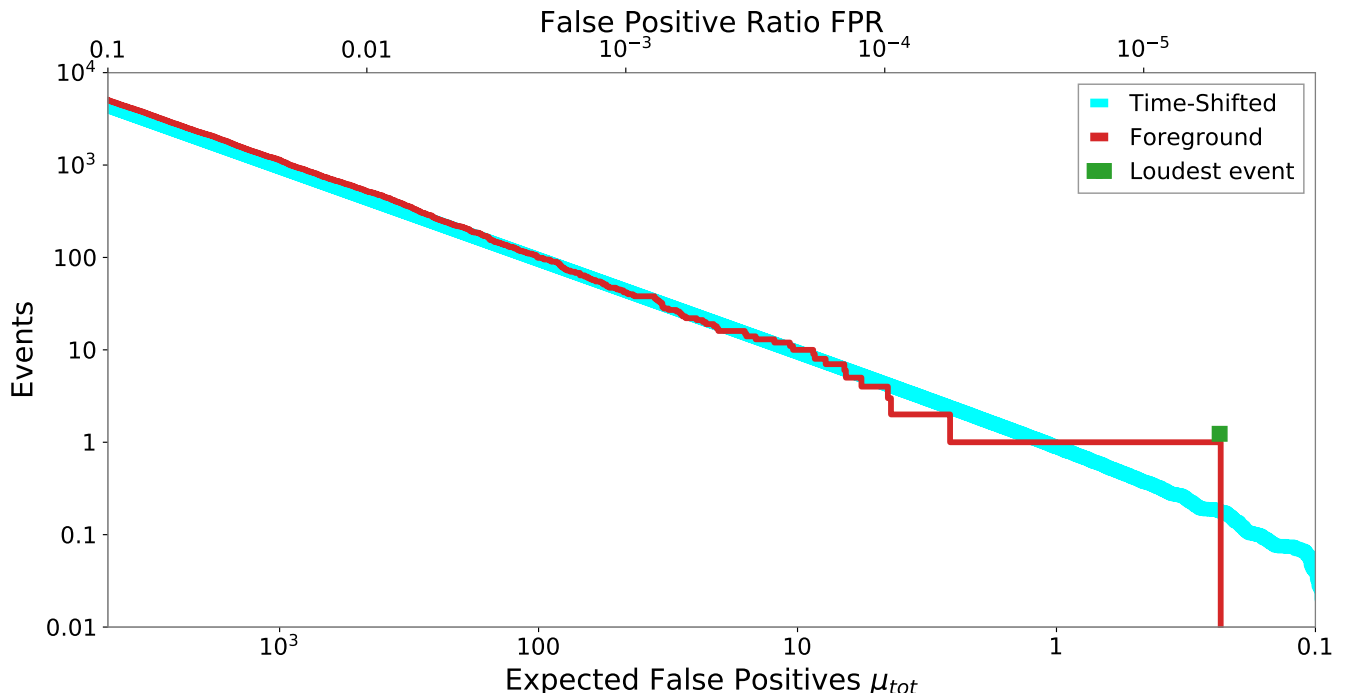


FIG. 9. The cumulative number of events above a given FPP [Eq. (29)] for both the time-shifted and foreground data. The mean number of false positives expected for each event is calculated with Eq. (32). The cumulative events for the time-shifted data was divided by the number of time-shifts to represent the average number of false positives expected for the foreground window. The tile with the smallest FPP, indicated by the green square, occurs with an FPP of 0.21 which corresponds to  $1.3\sigma$ .



## B. Limits

With no significant events detected, we determine a threshold  $\lambda_n^{th}$  for each box  $n$  corresponding to an expected value of one false positive over the dataset, i.e.  $FPR_n(\lambda_n^{th}) = 1/N_{tot}^{fg}$  [Eq. (32)]. These are then translated into a 90%-confidence upper limit on  $\mathcal{B}_p$  with the FC belts constructed for each box which are displayed in Fig. 10.

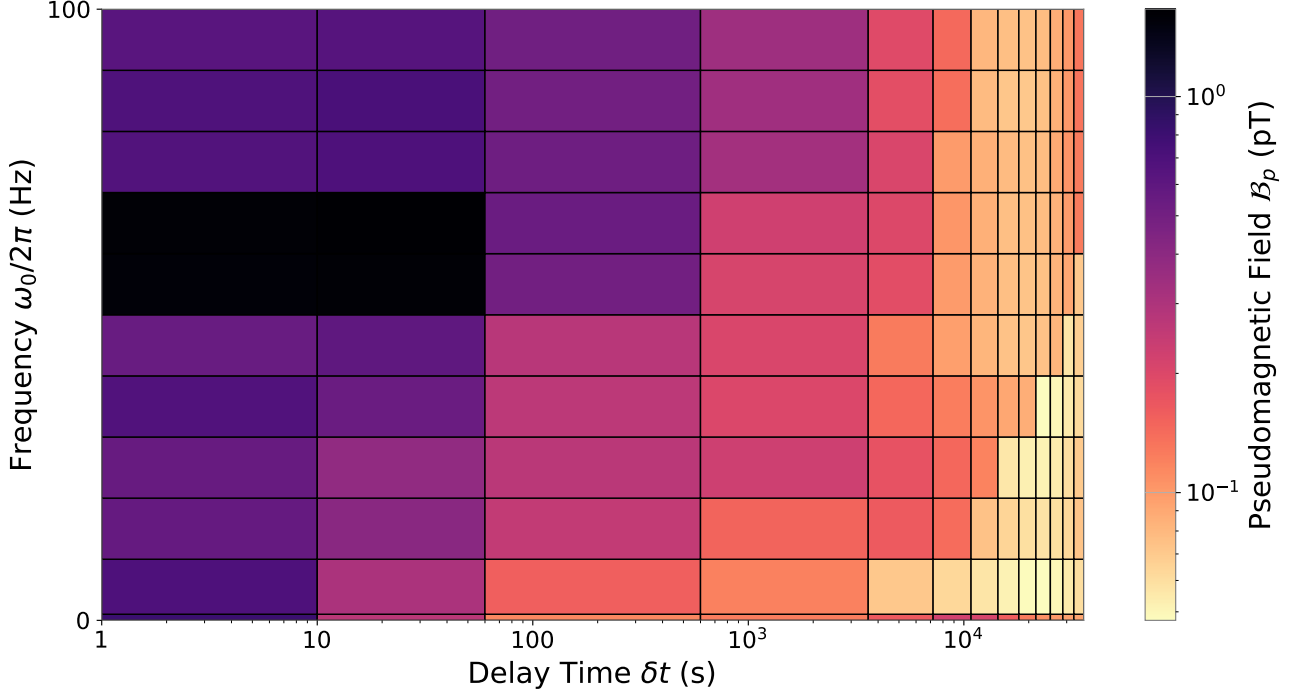


FIG. 10. Values of 90%-confidence upper limits of  $\mathcal{B}_p$  at  $\lambda_n^{th}$  for each time-frequency box shown in Fig. 4. The limits on  $\mathcal{B}_p$  are obtained by converting the threshold to a pseudomagnetic-field amplitude with the FC plot for each box. The network sensitivity strongly depends on the tile dimension deployed with longer time-averaged / narrower bandwidth tiles boasting higher sensitivity. The directional sensitivity of the network contributes to the increase in network sensitivity in the delay times between  $\sim 1 \times 10^4 - 3 \times 10^4$  s.

We determine the ELF mass range probed at each box from Eq. (4). The ELF mass

$$mc^2 = \hbar\omega_0 \sqrt{\frac{2c\delta t}{R}}, \quad (33)$$

depends on the central frequency  $\omega_0$ , the delay time  $\delta t$ , and the distance of the astrophysical event  $R$ . The dependence on the distance means that different search targets enable us to investigate different mass ranges, while the frequency and time delay dependence defines the mass band that we search for each target.

The 90%-confidence exclusion limits on the energy scale  $f^{l(q)}$  [Eqs. (15)-(16)] are determined with the 90%-confidence upper limit on  $\mathcal{B}_p$  and the center delay time and frequency of each box. Figure 11 displays the exclusion limits calculated for  $\tau_0 = 1$  s and  $\Delta E = 1 M_\odot c^2$ .

The exclusion limits can be calculated for other values of  $\Delta E$  by simply multiplying our presented results by  $\sqrt{\Delta E/M_\odot c^2}$ . The exclusion limits depend on  $\tau_0$  through Eq. (6), which depends on the delay time and frequency, and can be scaled to other values of  $\tau_0$  by recalculating  $\tau$  at the new value for each box. For all boxes, there is a limit on the initial burst duration,  $\tau_0 > 1/\omega_0$ , for the emitted energy spectra to be sufficiently sharp in frequency space [4].

Finally, we assume the ELF pulse and GW/EM trigger are emitted at the same time. If an alternative production theory postulates the time of emission of the ELFs and GW/EM differ then an appropriate offset should be added to the delay time.

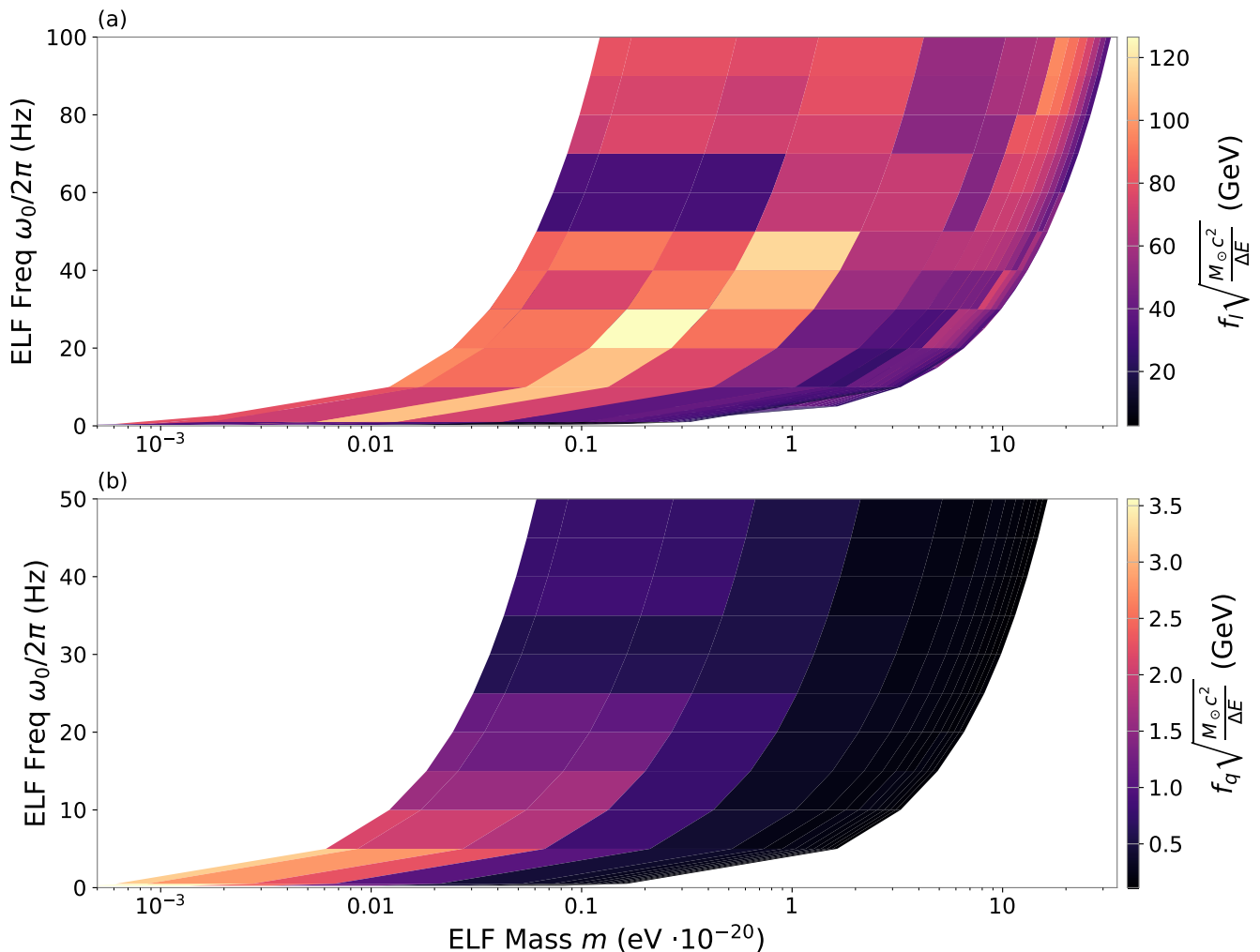


FIG. 11. 90% exclusion regions for (a) the linear energy scale  $f^l$  [Eq. (15)] and (b) the quadratic energy scale  $f^q$  [Eq. (16)] versus ELF mass [Eq. (33)] evaluated with  $\tau_0 = 1$  s,  $\Delta E = 1 M_\odot c^2$ , and the upper limits on  $\mathcal{B}_p$  for each box from Fig. 10. The signal from a quadratic interaction is at twice the central ELF frequency.

### C. Projected sensitivity to other events

We report limits from a single search target but investigating additional events will increase the coverage of ELF parameter space. Both the range of ELF masses [Eq. (33)] and energy scales [Eqs. (15)-(16)] that the network is sensitive to depend on the distance to the astrophysical event.

The GNOME collaboration is upgrading station sensors to co-magnetometers for the “Advanced GNOME” [16] that boast orders of magnitude higher sensitivity to ELF signals [31]. Figure 12 displays the projected sensitivity of this analysis to the ELF energy scales across a range of astrophysical distances. The curves are calculated for the approximate network sensitivity in this work and the projected network sensitivity of Advanced GNOME. The associated energy scales for linear and quadratic ELF interactions [Eqs. (15)-(16)] are evaluated at  $\tau_0 = 1$  s,  $\omega_0/2\pi = 1$  Hz, and  $\Delta E = 1 M_\odot c^2$  over a range of astrophysical distances. GNOME could search parameter space beyond the astrophysical limits with the next generation of co-magnetometer sensors.

## VI. CONCLUSIONS

We have developed an algorithm to search GNOME data for an exotic low-mass field burst copropagating with gravitational or electromagnetic signals from large-energy astrophysical events. We applied this analysis to data coincident

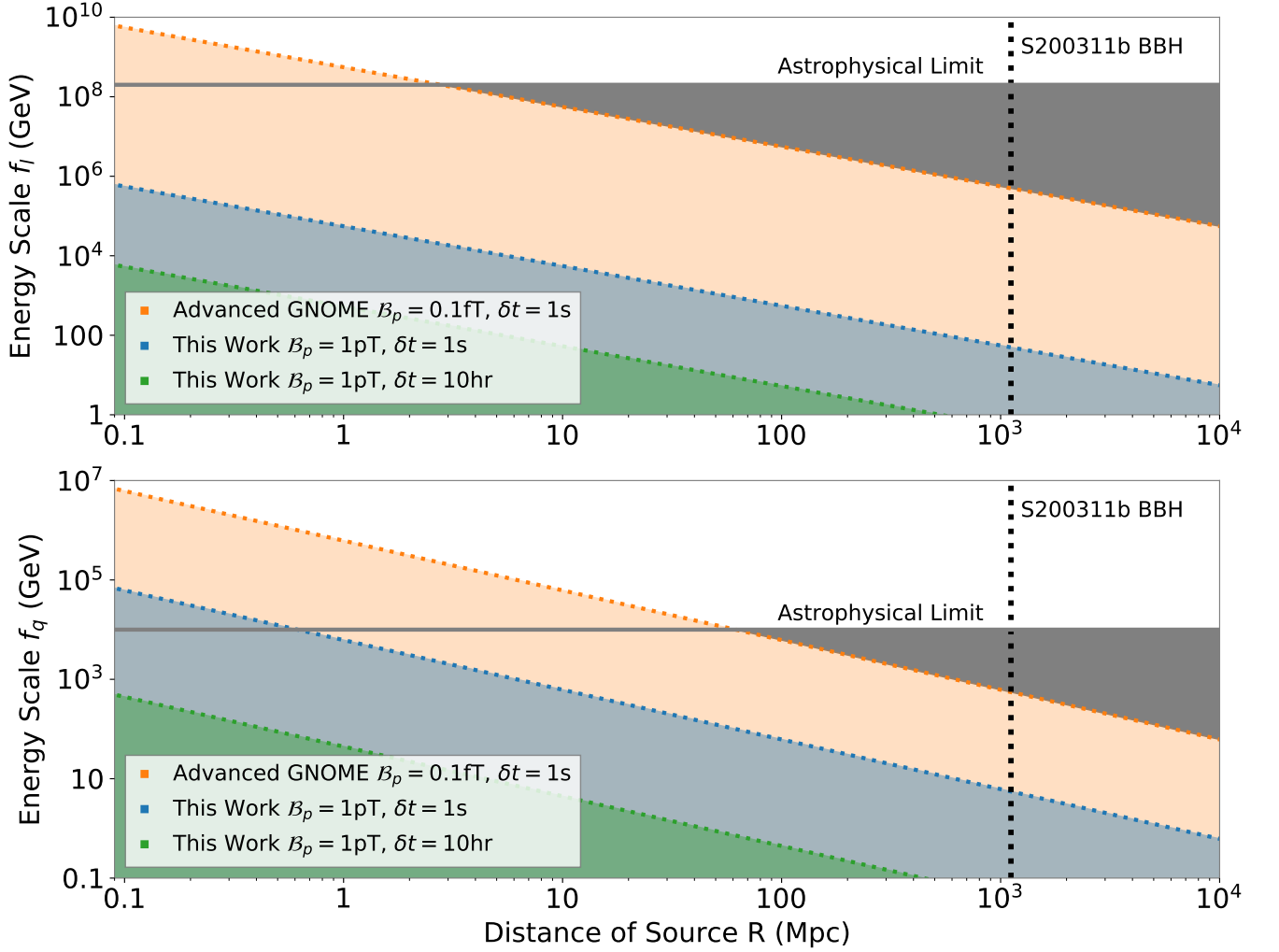


FIG. 12. Network sensitivity of this work and projected sensitivity of Advanced GNOME. The curves are Eqs. (15) and (16) calculated with  $\tau_0 = 1$  s,  $\omega_0/2\pi = 1$  Hz, and  $\Delta E = 1 M_\odot c^2$  for different values of  $\mathcal{B}_p$  and  $\delta t$ . The astrophysical limits on  $f_l$  and  $f_q$  are  $2 \times 10^8$  GeV [32] and  $1 \times 10^4$  GeV [33], respectively. The vertical dotted line indicates the distance to the BBH merger S200311b probed in this paper.

with the BBH merger S200311bg detected by LIGO/Virgo. No significant events were detected and we consequently placed the first lab-based constraints on combinations of ELF production and coupling parameters, namely the energy scales of the interaction between the ELF and proton spins, the energy released from the astrophysical event in the form of an ELF burst, and the initial ELF-burst duration.

This analysis will be applied to more GNOME datasets that are coincident with other gravitational-wave events detected by LIGO/Virgo and dozens of fast radio bursts. This will expand the mass range explored and closer events will allow higher energy scales to be probed. The collaboration is upgrading to self-compensating noble-gas-alkali-metal comagnetometers for implementation in the Advanced GNOME experiment. These improved sensors will be able to probe the coupling of exotic fields to protons and neutrons with higher sensitivity than our current sensors which can only probe the coupling to protons. Additionally, the response to magnetic and non-magnetic signals in the comagnetometers can be discriminated allowing for more efficient suppression of false positives. Furthermore, this analysis technique could be generalized to an all-sky search to hunt for potential signals without a known trigger.

## ACKNOWLEDGEMENTS

This work was supported by the U.S. National Science Foundation under grants PHY-1707875, PHY-1707803, PHY-2110370, PHY-2110388, and PHY-2207546; by the German Research Foundation (DFG) under grant no. 439720477 and within the German Excellence Strategy (Project ID 39083149); by work from COST Action COSMIC WISPerS CA21106, supported by COST (European Cooperation in Science and Technology)”; ZDG acknowledges institutional funding provided by the Institute of Physics Belgrade through a grant by the Ministry of Science, Technological Development and Innovations of the Republic of Serbia. The work of SP is supported by the National Science Centre of Poland within the Opus program (grant 2019/34/E/ST2/00440) and GL acknowledges the support of the Excellence Initiative – Research University of the Jagiellonian University in Kraków.

- 
- [1] J. Preskill, M. B. Wise, and F. Wilczek. Cosmology of the invisible axion. *Physics Letters B*, 120(1):127–132, 1983.
  - [2] L.F. Abbott and P. Sikivie. A cosmological bound on the invisible axion. *Physics Letters B*, 120(1):133–136, 1983.
  - [3] M. Dine and W. Fischler. The not-so-harmless axion. *Physics Letters B*, 120(1):137–141, 1983.
  - [4] C. Dailey et al. Quantum sensor networks as exotic field telescopes for multi-messenger astronomy. *Nature Astronomy*, 5(2):150–158, Feb 2021.
  - [5] G. G. Raffelt. Particle physics from stars. *Annual Review of Nuclear and Particle Science*, 49:163, 1999.
  - [6] D. Baumann, H. S. Chia, and R. A. Porto. Probing ultralight bosons with binary black holes. *Physical Review D*, 99(4):044001, 2019.
  - [7] I. I. Tkachev. Fast radio bursts and axion miniclusters. *Journal of Experimental and Theoretical Physics Letters*, 101:1, 2015.
  - [8] A. Arvanitaki, M. Baryakhtar, and X. Huang. Discovering the QCD axion with black holes and gravitational waves. *Physical Review D*, 91(8):084011, 2015.
  - [9] A. Arvanitaki, M. Baryakhtar, S. Dimopoulos, S. Dubovsky, and R. Lasenby. Black hole mergers and the QCD axion at Advanced LIGO. *Physical Review D*, 95(4):043001, 2017.
  - [10] M. Baryakhtar, R. Lasenby, and M. Teo. Black hole superradiance signatures of ultralight vectors. *Physical Review D*, 96(3):035019, 2017.
  - [11] M. Baryakhtar, M. Galanis, R. Lasenby, and O. Simon. Black hole superradiance of self-interacting scalar fields. *Phys. Rev. D*, 103(9):095019, 2021.
  - [12] Y. Fujii and K. Maeda. *The scalar-tensor theory of gravitation*. Cambridge Monographs on Mathematical Physics. Cambridge University Press, 2007.
  - [13] G. Franciolini, L. Hui, R. Penco, L. Santoni, and E. Trincherini. Effective field theory of black hole quasinormal modes in scalar-tensor theories. *J. High Energ. Phys.*, 2019(2):127, 2019.
  - [14] Virgo Collaboration LIGO Scientific Collaboration GCN 27358. 2020.
  - [15] D. F. Jackson Kimball and K. van Bibber. *The Search for Ultralight Bosonic Dark Matter*. Springer, 2022.
  - [16] S. Afach et al. What can a GNOME do? Search targets for the global network of optical magnetometers for exotic physics searches. *Annalen der Physik*, 531(1):2300083, 2023.
  - [17] S. Pustelny et al. The global network of optical magnetometers for exotic physics (GNOME): A novel scheme to search for physics beyond the standard model. *Annalen der Physik*, 525(8-9):659–670, 2013.
  - [18] S. Afach et al. Characterization of the global network of optical magnetometers to search for exotic physics (GNOME). *Physics of the Dark Universe*, 22:162–180, 2018.
  - [19] S. Afach et al. Search for topological defect dark matter with a global network of optical magnetometers. *Nature Physics*, 17(12):1396–1401, Dec 2021.
  - [20] D. Jackson Kimball et al. Magnetic shielding and exotic spin-dependent interactions. *Physical Review D*, 94(8):082005, 2016.
  - [21] S. S. Khamis, I. A. Sulai, P. Hamilton, et al. (unpublished).
  - [22] W. G. Anderson et al. Excess power statistic for detection of burst sources of gravitational radiation. *Physical Review D*, 63:042003, Jan 2001.
  - [23] F. E. James. *Statistical Methods in Experimental Physics; 2nd ed.* World Scientific, Singapore, 2006.
  - [24] G. J. Feldman and R. D. Cousins. Unified approach to the classical statistical analysis of small signals. *Phys. Rev. D*, 57:3873–3889, Apr 1998.
  - [25] M. Vetterli, J. Kovačević, and V. K. Goyal. *Foundations of Signal Processing*. Cambridge University Press, 2014.
  - [26] S. Chatterji, L. Blackburn, G. Martin, and E. Katsavounidis. Multiresolution techniques for the detection of gravitational-wave bursts. *Classical and Quantum Gravity*, 21(20):S1809, sep 2004.
  - [27] B. P. Abbott, The LIGO Scientific Collaboration, the Virgo Collaboration, et al. A guide to LIGO–Virgo detector noise and extraction of transient gravitational-wave signals. *Classical and Quantum Gravity*, 37(5):055002, feb 2020.
  - [28] M. Maggiore. *Gravitational Waves: Volume 1: Theory and Experiments*. Oxford University Press, New York, 2008.
  - [29] L. Lyons. Open statistical issues in particle physics. *Annals of Applied Statistics*, 2(3):887–915, September 2008.

- [30] R. Abbott et al. Gwtc-3: Compact binary coalescences observed by LIGO and Virgo during the second part of the third observing run. *Phys. Rev. X*, 13:041039, Dec 2023.
- [31] M. Padniuk et al. Universal determination of comagnetometer response to spin couplings. *Phys. Rev. Res.*, 6:013339, Mar 2024.
- [32] J. H. Chang, R. Essig, and S. D. McDermott. Supernova 1987a constraints on sub-gev dark sectors, millicharged particles, the QCD axion, and an axion-like particle. *Journal of High Energy Physics*, 2018(9):51, Sep 2018.
- [33] M. Pospelov et al. Detecting domain walls of axionlike models using terrestrial experiments. *Physical Review Letters*, 110(2):021803, 2013.